ADVANCED OPTICAL MATERIALS
www.advopticalmat.de

Inverse-Designed Dispersive Time-Varying Nanostructures

Puneet Garg, Jan David Fischbach, Aristeidis G. Lamprianidis, Xuchen Wang, Mohammad S. Mirmoosa, Viktar S. Asadchy, Carsten Rockstuhl,* and Thomas J. Sturges**

Time-varying nanostructures allow to control the spatial and temporal properties of light. The temporal modulation of the nanostructures constitutes an additional degree of freedom to control their scattering properties on demand and in a reconfigurable manner. However, these additional parameters create a vast design space, raising challenges in identifying optimal designs. Therefore, tools from the field of photonic inverse design must be used to optimize the degrees of freedom of the system to facilitate predefined optical responses. To further develop this field, here a differentiable transition (T-) matrix-based inverse design framework is introduced for dispersive time-varying nanostructures. The electron density of the material of the nanostructures is modulated non-adiabatically as a generic periodic function of time. Using the inverse design framework, the temporal shape of the electron density can be manipulated to reach the target functionality. This computational framework is exploited, exemplarily, in two instances. First, the decay rate enhancement of oscillating dipoles near time-varying spheres is controlled on demand. Second, using spatiotemporal metasurfaces, a system supporting asymmetric transmission of light at visible frequencies is designed. This work paves the way toward programmable spatiotemporal metasurfaces and space-time crystals for a future generation of reconfigurable functional photonic devices.

1. Introduction

Time-varying nanostructures facilitate the simultaneous manipulation of light's spatial and temporal properties.[1] In this context, time modulation refers to changing the material properties as a function of time.[2–4] Additionally, in the case of nanostructures, we consider spatially localized structured objects. Recently, various applications exploiting time-varying media have been reported. Some of them are made from spatially homogeneous, and some of them are made from spatially structured materials. These applications include parametric amplification,[5,6] nonreciprocal light propagation,[7,8] asymmetric frequency conversion,[9] power combining of waves,[10] temporal aiming,[11] inverse prisms,[12] wave freezing,[13] anti-reflection temporal coatings,[14,15] perfect absorption,[16,17] polarization conversion,[9,18,19] spatiotemporal wavefront shaping,[20] and so forth. Besides, various experimental advancements in the field of time-varying materials have fueled the interest of the photonics community in this research domain.[21–27] Owing to the tunability of the temporal modulation, several reconfigurable devices with desired functionalities can be realized using such dynamic materials.[26,28,29] It has to be emphasized that the ability to drastically change the optical response of photonic structures after fabrication is in striking contrast to most conventional systems whose properties are fixed upon fabrication. Of course, multiple other approaches exist to tune the optical response after fabrication, but a temporal modulation seems to be particularly versatile.

Generally, the temporal modulation unlocks additional degrees of freedom to control the flow of light. However, these

P. Garg, A. G. Lamprianidis, C. Rockstuhl, T. J. Sturges
Institute of Theoretical Solid State Physics
Karlsruhe Institute of Technology
Kaiserstr. 12, 76131 Karlsruhe, Germany
E-mail: puneet.garg@kit.edu; carsten.rockstuhl@kit.edu; thomas.sturges@kit.edu

J. D. Fischbach, C. Rockstuhl
Institute of Nanotechnology
Karlsruhe Institute of Technology
Kaiserstr. 12, 76131 Karlsruhe, Germany

The ORCID identification number(s) for the author(s) of this article can be found under https://doi.org/10.1002/adom.202402444

DOI: 10.1002/adom.202402444

X. Wang
Qingdao Innovation and Development Base
Harbin Engineering University
Qingdao 266400, China

M. S. Mirmoosa
Department of Physics and Mathematics
University of Eastern Finland
Joensuu P.O. Box 111, FI-80101, Finland

V. S. Asadchy
Department of Electronics and Nanoengineering
Aalto University
Espoo P.O. Box 15500, FI-00076, Finland

additional parameters are a blessing and a curse in that they create a vast design space but simultaneously challenge the identification of optimal designs. It prompts the use of tools from the field of photonic inverse design, a framework well established by now to design optical devices with tailored functionality.[30–33] Generally, photonic inverse design is used to iteratively optimize the parameters of a nanostructure toward a design that fulfills a predefined optical functionality.[30] It frequently utilizes fully differentiable software tools that incorporate built-in adjoint solvers, allowing for the optimization of devices with numerous design parameters through a gradient-based method.

Photonic inverse design has already been used to engineer the interaction of light with time-varying systems. Examples include optical pulse shaping for their enhanced interaction with temporally periodic media,[34] unidirectional scattering from disordered photonic time crystals,[35] topological state design for photonic time crystals,[36] non-reciprocal light propagation from spatiotemporal nanostructures,[37] and spectral control of light from time-varying dispersionless spheres.[38] It is important to remark that most materials, whose properties can be modulated as a function of time with modulation frequencies comparable to the oscillation frequency of light (i.e., non-adiabatic modulation), exhibit dispersion in the optical regime.[39–41] However, to the best of the authors' knowledge, a study involving the photonic inverse design of dispersive and non-adiabatically modulated optical nanostructures has not yet been reported.

To effectively use the techniques from the field of photonic inverse design, the forward problem needs to be solved efficiently at first. Using traditional full-wave Maxwell solvers to model such nanostructures, e.g., based on the finite-element method, is often computationally expensive.[42,43] However, a particularly useful formalism to model such nanostructures efficiently is the transition matrix (also known as the T-matrix) formalism.[44] The T-matrix encapsulates the linear scattering response of the considered nanostructure. Once the T-matrix is known, we can calculate the field scattered off the nanostructure for an arbitrary illumination. In fact, given the T-matrix of a finite scatterer, one can compute the effective T-matrix of an infinite periodic arrangement of such a scatterer using the Ewald summation technique.[45,46] That approach allows us to study the optical response from spatiotemporal metasurfaces. Furthermore, the T-matrix model can be made differentiable, enabling gradient-based optimization techniques to be applied to designing the underlying nanostructures.

In this article, we propose a differentiable T-matrix-based inverse design framework that incorporates material dispersion and non-adiabatic temporal modulations. Our framework can handle time-varying spheres and spatiotemporal metasurfaces made from such spheres. We assume the underlying material of the spheres to have a generic time-periodic electron density. We model these time-varying nanostructures using the differentiable T-matrix formalism. Moreover, we use a gradient-based optimization technique to tailor the scattering characteristics of the nanostructures on demand. In particular, we optimize the temporal profile of the electron density of the underlying material to reach the desired optical responses for the nanostructures. Utilizing the proposed inverse design framework, we showcase its applicability in two key examples. First, we design the electron density of the material of a sphere such that a dipole near it exhibits anomalous Drexhage effect. Second, we design the electron density of the material of a spatiotemporal metasurface that leads to an efficient frequency upconversion in transmission. This metasurface is then cascaded with a narrow-band frequency filter to realize the asymmetric transmission of light. Importantly, the parameters of the system are chosen so that asymmetric transmission is achieved for visible light.

2. Inverse Design Framework

In this section, the optimization framework used to design the time-varying nanostructures is presented (see **Figure 1**). In principle, there are many possible approaches. Global optimization techniques such as Bayesian optimization[47] and particle swarm optimization[48] constitute powerful tools for optimizing complicated objective functions (such as ours). However, they scale quite poorly with the number of design parameters. Deep learning approaches are also possible.[49,50] However, the computational costs of generating a suitable training dataset are relatively high, making this approach undesirable in situations where only a few individual optimizations are needed. For all these reasons, we choose automatic differentiation in combination with a local gradient-based optimization algorithm to design our structures. This autodiff approach allows us to efficiently find optimized designs with a computational cost that is independent of the number of design variables, making this a very scalable approach. While there is no guarantee of converging to the global optimum, many locally optimal solutions often yield satisfactory designs. Consequently, for practical purposes, local gradient-based optimization serves as an efficient and effective tool for inverse design. We note that our approach is conceptually similar to "adjoint optimization."[51,52] However, our autodiff approach gives us the exact gradients of the discretized system, at the cost of a significantly higher memory requirement. We begin by outlining the differentiable T-matrix method used for modeling time-varying nanostructures. Then, we describe the gradient-based optimization procedure.

2.1. Differentiable T-Matrix Method

In this article, we optimize the optical properties of time-varying spheres and spatiotemporal metasurfaces (see Figure 1a). The considered spatiotemporal metasurfaces are periodic arrays of time-varying spheres arranged in two dimensions (2D). We assume these nanostructures to be made from a dispersive material whose electron density $N(t)$ is a periodic function of time, with a period of $\tau_{\mathrm{m}} = 2\pi/\omega_{\mathrm{m}}$. Here, we consider the non-adiabatic modulation regime, where ω_{m} is comparable to the oscillation frequency of light. Such a time-varying electron density $N(t)$ is incorporated into our analysis using the Drude dispersion model[42,43] (see Section S1, Supporting Information). Note that for all the examples in this manuscript, we use Drude parameters that resemble the properties of gold at frequencies below its plasma frequency.[53] Such a choice is made as gold exhibits strong dispersion at visible frequencies that are of interest in this work. Importantly, due to the time modulation of the nanostructures, an incident excitation with frequency ω gives rise to a polychromatic scattered field with frequencies $\omega_j = \omega + j\omega_{\mathrm{m}}$, with $j \in \mathbb{Z}$ (see Figure 1a).

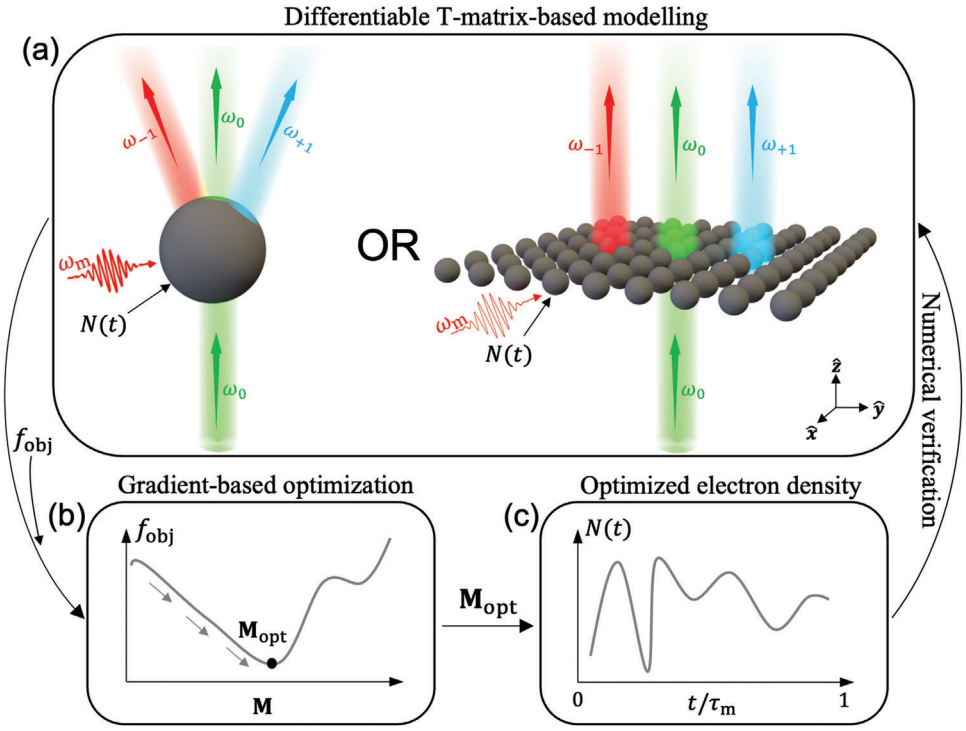

Figure 1. Inverse design framework. First, a time-varying sphere or spatiotemporal metasurface, as shown in (a), is numerically set up using the differentiable T-matrix-based model. Then, depending on the desired functionality of the considered nanostructure, an objective function $f_{\text{obj}}(\mathbf{M})$ is defined. The time variance of the nanostructure is encoded in the Fourier coefficients $\mathbf{M}$ of the electron density $N(t)$. Next, f_{obj} is minimized or maximized using gradient-based optimization as shown in (b). The optimization returns the optimal Fourier coefficients $\mathbf{M} = \mathbf{M}_{\text{opt}}$ that correspond to an optimal time-varying electron density $N(t)$ shown in (c). Finally, the optimization results are numerically verified for the desired functionality by a forward simulation of the considered nanostructure having the optimal $N(t)$. Here, $\tau_{\text{m}} = 2\pi/\omega_{\text{m}}$ corresponds to the period of the temporal modulation.

As mentioned earlier, linear optical nanostructures can be numerically modeled using the T-matrix method.[44] The T-matrix is an efficient tool to semi-analytically model optical nanostructures based on Mie theory.[54] It can handle finite scatterers and photonic materials made from an infinite periodic arrangement of such scatterers. The T-matrix formalism involves expanding the incident field $\mathbf{E}^{\text{inc}}$ and scattered field $\mathbf{E}^{\text{sca}}$ for the nanostructure in a basis of vector spherical harmonics (see the Methods Section). Let $\mathbf{A}^{\text{inc}}$ and $\mathbf{A}^{\text{sca}}$ be the corresponding incident and scattered coefficient vectors, respectively. Then, $\mathbf{A}^{\text{inc}}$ and $\mathbf{A}^{\text{sca}}$ satisfy

$$\mathbf{A}^{\text{sca}} = \mathbf{T} \cdot \mathbf{A}^{\text{inc}} \tag{1}$$

where $\mathbf{T}$ is the so-called T-matrix of the considered nanostructure. From Equation (1), we note that the T-matrix completely encapsulates the scattering response of the nanostructure. Once the T-matrix of the nanostructure is known, the field scattered off it can be calculated easily using Equation (1). The T-matrix for static scatterers can be computed analytically or using full-wave Maxwell solvers.[55–57] Note that the T-matrix formalism is closely related to the widely used scattering matrix (S-matrix) formalism. In fact, once the T-matrix of a nanostructure is known, its S-matrix can be calculated by performing appropriate basis transformations as shown in Section S2 (Supporting Information). Recently, the T-matrix formalism has also been applied to time-varying nanostructures.[38,42,43,58–60] The T-matrices of dispersive time-varying spheres and spatiotemporal metasurfaces made from these time-varying spheres are analytically known.[42,43] We use these existing T-matrices for our purposes. We wish to highlight here that Equation (1) also holds for the time-varying nanostructures. In that case, the size of $\mathbf{T}$ depends on the number of scattered frequencies ω_j and considered vector spherical harmonics (see the Methods Section). Furthermore, it is important to mention that we wrote our T-matrix-based code using JAX, a software package that can automatically differentiate native Python and Numpy functions.[61] Therefore, it makes our T-matrix model differentiable, allowing us to use a gradient-based optimization as discussed in the following.

2.2. Optimization Procedure

Having established the differentiable T-matrix-based model, we next discuss the optimization procedure. We use a gradient-based optimization approach. We begin by expanding $N(t)$ in a Fourier series. Such an expansion of $N(t)$ in a Fourier series is done as we solve the problem in the frequency domain in our computational framework. Therefore, $N(t)$ can be written as

$$N(t) = N_0 \left[1 + \sum_{q=1}^{Q} \left(M_q e^{-iq\omega_{\text{m}} t} + \text{c.c.} \right) \right] \tag{2}$$

Here, N_0 corresponds to the electron density of the static material, the different M_q correspond to the complex Fourier

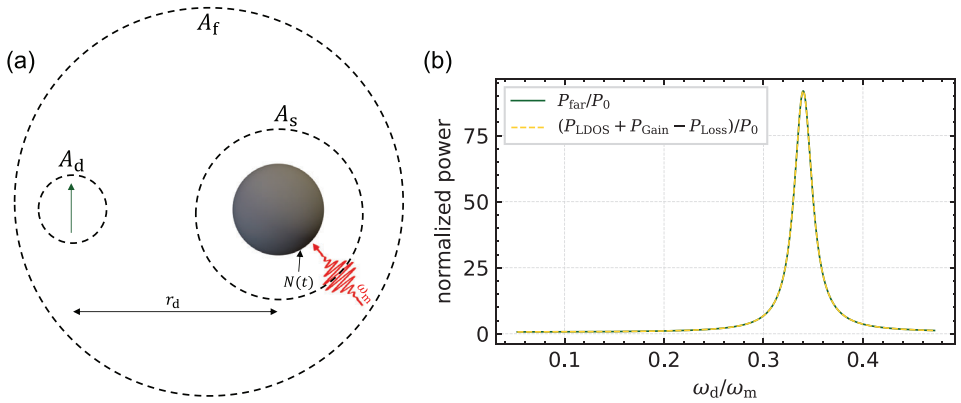

Figure 2. a) A system consisting of an electric dipole near a time-varying sphere. b) Normalized powers plotted as a function of the emission frequency ω_d of the dipole for the system shown in (a). Here, the time-varying electron density of the sphere is given by $N(t) = N_0[1 + 0.8\cos(\omega_m t)]$, and its radius is $R = 10$ nm. Furthermore, the dipole is kept at a distance $r_d = 15$ nm from the center of the sphere. Moreover, $\omega_m = 0.17c_0/R$ with c_0 being the speed of light in a vacuum.

coefficients of $N(t)$, Q is the total number of considered M_q coefficients, and c.c. refers to the complex conjugate. The electron density $N(t)$ is non-negative and real-valued. We define a vector $\mathbf{M}$ that contains all the coefficients M_q for brevity. Then, depending on the desired functionality of the time-varying nanostructure, an objective function $f_{obj}(\mathbf{M})$ is defined. The objective function f_{obj} takes $\mathbf{M}$ as the design variables. Note that the base modulation frequency ω_m is chosen a priori and does not enter the optimization procedure.

Next, depending on the design goal, f_{obj} is either minimized or maximized using gradient-based optimization (see Figure 1b). As mentioned earlier, the differentiable T-matrix-based model allows us to compute the derivatives of f_{obj} with respect to $\mathbf{M}$. Additionally, thanks to the reverse-mode automatic differentiation, we obtain the derivatives of f_{obj} with respect to all $M_q \in \mathbf{M}$ with a single backward pass through the simulation.[62] More details on the software packages can be found in Subsection S3.1 (Supporting Information). Using the gradient information, we iteratively update $\mathbf{M}$ until a local minimum/maximum of f_{obj} is reached (see Figure 1b). Such an optimization returns the optimal Fourier coefficient vector $\mathbf{M} = \mathbf{M}_{opt}$, and correspondingly, the optimal time-varying electron density $N(t)$ (see Figure 1c). Finally, we numerically verify if the desired functionality is reached by running a forward simulation with the optimal $N(t)$ (see Figure 1a). Note that the details of various convergence parameters used for calculations in this manuscript are available in the Supporting Information.

Having introduced the inverse design framework, we now exploit it to study two distinct phenomena. First, we tailor the electron density of the material of a time-varying sphere so that a dipole in its vicinity displays anomalous Drexhage effect. Next, we present an example based on the spatiotemporal metasurfaces to realize asymmetric transmission of light at visible frequencies.

3. Radiative Decay Rate Enhancement

Nanostructures are extensively used in the photonics community to enhance the spontaneous radiative decay rates of excited atoms.[63–65] In classical theory, an excited atom can be modeled as an oscillating point electric dipole.[66] Recently, there has been a growing interest in studying the spontaneous decay rates of dipoles in the vicinity of time-varying media.[67–70] Time-varying media are non-Hermitian systems, as they can supply (leading to optical gain) and absorb (leading to optical loss) energy to and from the incident electromagnetic fields. However, optical gain necessitates a careful examination of the existing approaches to calculate the decay rates of dipoles near such non-Hermitian systems.[71,72] Therefore, for the dipoles in the vicinity of time-varying nanostructures, the effects of optical gain on their spontaneous decay rate calculation must be considered. The optical gain can be interpreted as a spontaneous excitation of the atom from its ground to an excited state, eventually leading to the subsequent emission of a photon.[69,71] Here, the excitation of the atom is not photon-mediated; rather it occurs due to the non-adiabatic quantum pumping induced by the time-periodic material.[69,71] Note that non-adiabatic quantum pumping is a process where a system, due to rapid time modulation, cannot respond instantaneously and consequently ceases to remain in its ground state.[73] The calculation of the decay rates of dipoles in the vicinity of time-periodic media has been shown in various works.[67–70] However, a computation of the decay rates of dipoles kept near spatially finite time-varying media has not yet been presented. Finite media are advantageous as they allow greater flexibility in positioning the dipoles near them. In the following, using the arguments of ref. [72], we derive an expression for the radiative decay rate enhancement of a dipole kept near a time-varying sphere while considering the optical gain (and loss) from the sphere.

3.1. Derivation of the Radiative Decay Rate Enhancement

The power conservation relation for a dipole kept in the vicinity of an arbitrary active (gain providing) and an arbitrary absorbing resonator reads as [[72], Equation (21)]

$$P_{far} = P_{LDOS} + P_{gain} - P_{abs} \tag{3}$$

Here, P_{far} refers to the total power radiated by the system formed by the dipole and the resonators in the far field, P_{LDOS} refers to the net power crossing an imaginary surface enclosing only the dipole, P_{gain} refers to the total power gained by the system due to the active resonator, and P_{abs} refers to the total power absorbed by the lossy resonator from the system. Note that, in our analysis, time-averaged powers are considered (see Section S5, Supporting Information).

We aim to derive an expression for the radiative decay rate enhancement of a dipole kept near a time-varying sphere (see **Figure 2a**). As mentioned earlier, a time-varying sphere acts as a medium that can supply and absorb energy to and from the fields incident on it. As Equation (3) holds for dipoles near arbitrary gain-loss resonators, it must also hold for a system consisting of a dipole kept near a time-varying sphere. However, Equation (3) was initially written for dipoles near static gain media.[72] Therefore, it must be first verified for the system involving time-varying media. To test Equation (3), we plot the values of the left and right-hand sides independently as a function of the emission frequency ω_d of the dipole in Figure 2b. In the context of such a sphere-dipole system, P_{far}, P_{LDOS}, and $P_{gain} - P_{loss}$ refer to the net powers crossing the surfaces A_f, A_d, and A_s, respectively (see Figure 2a). Here, A_f, A_d, and A_s correspond to the surfaces enclosing both the sphere and dipole, only the dipole, and only the sphere, respectively. Note that we use the T-matrix method to calculate these powers (see Section S4, Supporting Information). Furthermore, in Figure 2b, the plotted powers are normalized by the power P_0 radiated by the dipole in a vacuum. From Figure 2b, we observe that the power conservation relation given in Equation (3) also holds for the sphere-dipole system. Next, the gain corrected expression for the total emitted power by the dipole P^{dip}_{total} that is responsible for its spontaneous decay in the presence of such a non-Hermitian sphere is,[72] [Equation (23)]

$$P^{dip}_{total} = P_{LDOS} + P_{gain} \tag{4}$$

Moreover, using Equations (3) and (4), we can write $P_{far} = P^{dip}_{total} - P_{abs}$. Note that $P^{dip}_{total} - P_{abs}$ corresponds to the net radiatively emitted power from the dipole P^{dip}_{rad} that leads to its spontaneous *radiative* decay.[74,75] Therefore, we conclude that $P_{far} = P^{dip}_{rad}$. Finally, the radiative decay rate enhancement γ_{rad}/γ_0 of the dipole kept near a time-varying sphere can be written as

$$\frac{\gamma_{rad}}{\gamma_0} = \frac{P^{dip}_{rad}}{P_0} = \frac{P_{far}}{P_0} \tag{5}$$

Here, γ_{rad} refers to the radiative decay rate of the dipole in the presence of the time-varying sphere, and γ_0 refers to the decay rate of the dipole in a vacuum.

Having discussed the details of decay rate calculation, we proceed to apply our inverse design framework to engineer the radiative decay rate enhancement of the dipoles near time-varying spheres on demand.

3.2. Anomalous Drexhage Effect

In 1970, K.H. Drexhage showed that the radiative decay rate enhancement of a dipole kept near a perfect mirror depends on the orientation of the dipole to the surface of the mirror.[76] A similar effect is observed for a dipole near a *static* sphere, as shown in **Figure 3a**. Here, we plot the radiative decay rate enhancement γ_{rad}/γ_0 of an electric dipole for its two orthogonal polarizations as a function of the distance r_d from the center of a static sphere. Note that $\perp$-polarization refers to the radial and $\parallel$-polarization refers to the tangential orientation of the dipole with respect to the sphere. The radius of the sphere is $R = 10$ nm, and the emission frequency of the dipole is $\omega_d = 0.072 c_0/R$. Here, c_0 is the speed of light in a vacuum.

From Figure 3a, we observe that the decay rate enhancement shows different trends as a function of the distance r_d for the two orientations of the dipole. Consider the regime $r_d/R \approx 1$. For the tangential orientation, the decay rate is almost negligible leading to $\gamma_{rad}/\gamma_0 \approx 0$. In contrast, the decay rate is significant for the radial orientation leading to $\gamma_{rad}/\gamma_0 \gg 1$. Such an orientation-dependent decay rate enhancement of the dipole is known as the Drexhage effect.[76]

The physical explanation for the Drexhage effect is as follows. To begin with, the decay rate enhancement of the dipole depends on the total far field[74,77] (see Equation (5)). The total far field $\mathbf{E}^{tot}(\mathbf{r}_{far})$ is the sum of the field scattered from the sphere $\mathbf{E}^{sca}(\mathbf{r}_{far})$ and the field of the dipole itself $\mathbf{E}^{dip}(\mathbf{r}_{far})$, in the absence of the sphere, at a spatial location $\mathbf{r} = \mathbf{r}_{far}$. Here, $r_{far} \gg R$. For the example shown in Figure 3a, $\mathbf{E}^{sca}$ and $\mathbf{E}^{dip}$ interfere destructively (constructively) for the tangential (radial) orientation of the dipole leading to negligible (significant) decay rate enhancement. Besides, for $r_d/R \gg 1$, for both the orientations of the dipole, γ_{rad}/γ_0 saturates to unity. This saturation happens because $\mathbf{E}^{sca}$ decays rapidly as r_d increases, leading to a decrease in the interference effects of the fields and consequently the impact of the sphere on γ_{rad}.[74] Therefore, γ_{rad} approaches γ_0 for $r_d/R \gg 1$.

Having discussed the Drexhage effect, we explore the anomalous Drexhage effect next. It refers to a situation where a dipole shows a similar decay rate enhancement for its two orthogonal orientations. This is considered here as anomalous because it is in striking contrast to the Drexhage effect that has been studied from multiple perspectives.[78,79] Our goal is to show such an anomalous Drexhage effect by an appropriate time modulation of the sphere. To do so, we design the time-varying electron density $N(t)$ of the sphere such that, even for the tangential orientation of the dipole, we have a significant decay rate enhancement for $r_d/R \approx 1$. Therefore, we maximize γ_{rad}/γ_0 for $r_d/R \approx 1$ for the tangential orientation of the dipole. From Equation (5), we observe that γ_{rad}/γ_0 is proportional to the power emitted in the far field by the sphere-dipole system P_{far}. Consequently, our task at hand is reduced to maximizing P_{far} when the dipole is placed sufficiently close to the sphere. We choose $r_d = 1.01R$.

To set up the optimization problem, we define our objective function f_{obj} in terms of P_{far} (see the Methods Section). Note that besides P_{far}, f_{obj} also consists of a penalty function that penalizes the optimizer if $N(t)$ tends toward negative values for any $t \in [0, \tau_m]$. We use such a penalty function with all other objective functions in this article. Additionally, we need to fix the base modulation frequency ω_m a priori in the optimization. To choose ω_m such

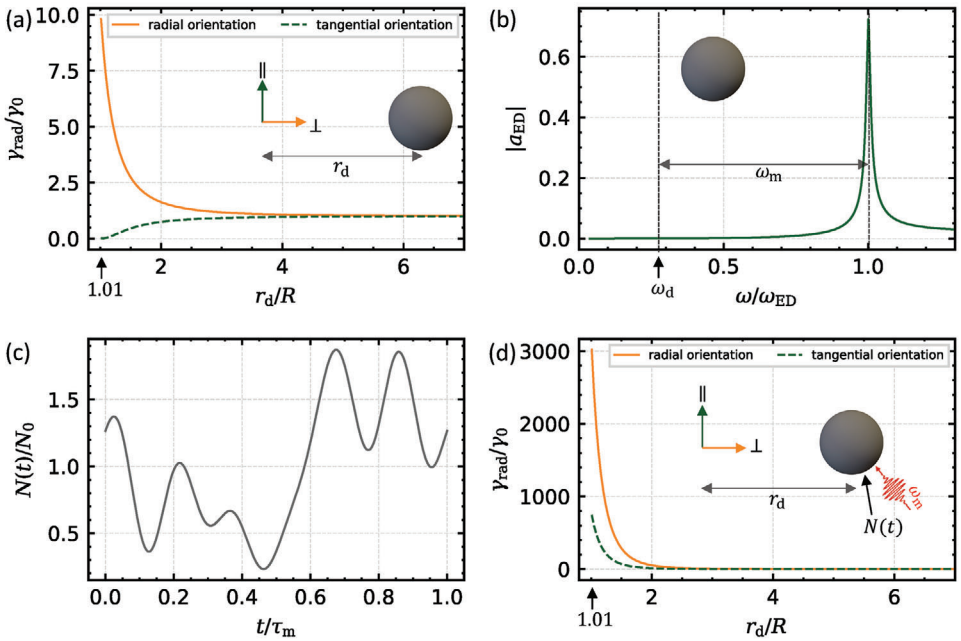

Figure 3. Anomalous Drexhage Effect. a) The radiative decay rate enhancement γ_{rad}/γ_0 for an electric dipole as a function of its distance r_d from the center of a static sphere for its two orthogonal polarizations. b) The absolute value of the electric dipolar Mie coefficient of the static sphere as a function of the excitation frequency ω. c) The optimized electron density $N(t)$ that maximizes γ_{rad}/γ_0 for the tangentially orientated dipole (||- polarization) at $r_d/R = 1.01$. d) The radiative decay rate enhancement γ_{rad}/γ_0 of the dipole in two orthogonal polarizations as a function of its distance r_d from the time-varying sphere having the optimized $N(t)$ shown in (c).

that it assists the maximization of P_{far}, we first plot the amplitude of the electric dipolar Mie coefficient a_{ED} of the static sphere as a function of the excitation frequency ω[80] (see Figure 3b). From Figure 3b, we observe the existence of the electric dipolar resonance of the sphere at $\omega = \omega_{ED}$. Therefore, we choose $\omega_m = \omega_{ED} - \omega_d$. Such a choice is made because once the time modulation is turned on, the sphere in the presence of the dipole emitting at the frequency ω_d scatters the frequencies $\omega_j = \omega_d + j\omega_m$, with $j \in \mathbb{Z}$ (see Figure 1a). Therefore, $\omega_1 = \omega_{ED}$ lies exactly at the electric dipolar resonance frequency leading to a resonant enhancement of P_{far} in the time-varying case for an appropriately optimized $N(t)$ (see Equation (S6), Supporting Information).

Having chosen f_{obj} and ω_m, we use the inverse design framework discussed in Section 2 to maximize γ_{rad}/γ_0 for the dipole oriented tangentially to the time-varying sphere at $r_d = 1.01R$. The optimized $N(t)$ is shown in Figure 3c. Note that within our optimization landscape, there exist different temporal profiles that provide similar results. Ultimately, our goal is to obtain a design that fulfills our objective. Thus, any such solution is suitable. This conclusion also holds for all other optimization results presented in this work. Furthermore, in Figure 3d, we plot γ_{rad}/γ_0 as a function of r_d for the dipole near the time-varying sphere. From Figure 3d, we observe that for both the tangential and radial orientation of the dipole, the decay rate enhancement is significant (i.e., $\gamma_{rad}/\gamma_0 \gg 1$) for $r_d/R \approx 1$, leading to a demonstration of the anomalous Drexhage effect.

In particular, as intended, the optimization successfully returns an $N(t)$ that maximizes γ_{rad}/γ_0 when $r_d/R \approx 1$ for the tangential orientation of the dipole. Such a maximization can be explained as follows. As expected, the temporal modulation with the optimized $N(t)$ enhances the total far field $\mathbf{E}^{tot}(\mathbf{r}_{far})$ at $\omega_j = \omega_1$ (see Section S6, Supporting Information). Moreover, since the power P_{far} depends on the contributions of $\mathbf{E}^{tot}(\mathbf{r}_{far})$ across all the frequencies ω_j, this field enhancement at ω_1 maximizes P_{far}, which in turn maximizes the decay rate enhancement. Additionally, even for the radial orientation of the dipole, γ_{rad}/γ_0 at $r_d/R \approx 1$ is about 300 times higher in the time-varying case than that in the static case. Such a high γ_{rad}/γ_0 for the radial orientation also occurs due to a similar total far field enhancement.

It is worth remarking that in order to instead suppress γ_{rad} for the radial orientation of the dipole shown in Figure 3a, one needs to reduce P_{far} sufficiently (see Equation (5)). One possible way to achieve this is to enhance the absorptivity of the sphere using time modulation.[16,17] In the limiting case when the sphere acts as a perfect absorber, P_{far} vanishes, leading to a complete suppression of γ_{rad}.

As discussed in the following, we now apply our inverse design framework to a system involving spatiotemporal metasurfaces.

4. Asymmetric Transmission of Light at Visible Frequencies

As the second application of our inverse design framework, we design a device that implements asymmetric transmission (AT) of light at visible frequencies. A device operating under the AT condition allows efficient transmission of light in one direction while blocking it in the opposite direction.[81] A conceptual illustration of spatiotemporal metasurface-based AT is shown in **Figure 4a**. The system shown in Figure 4a is formed by cascading a spatiotemporal metasurface and a narrow-band frequency filter.

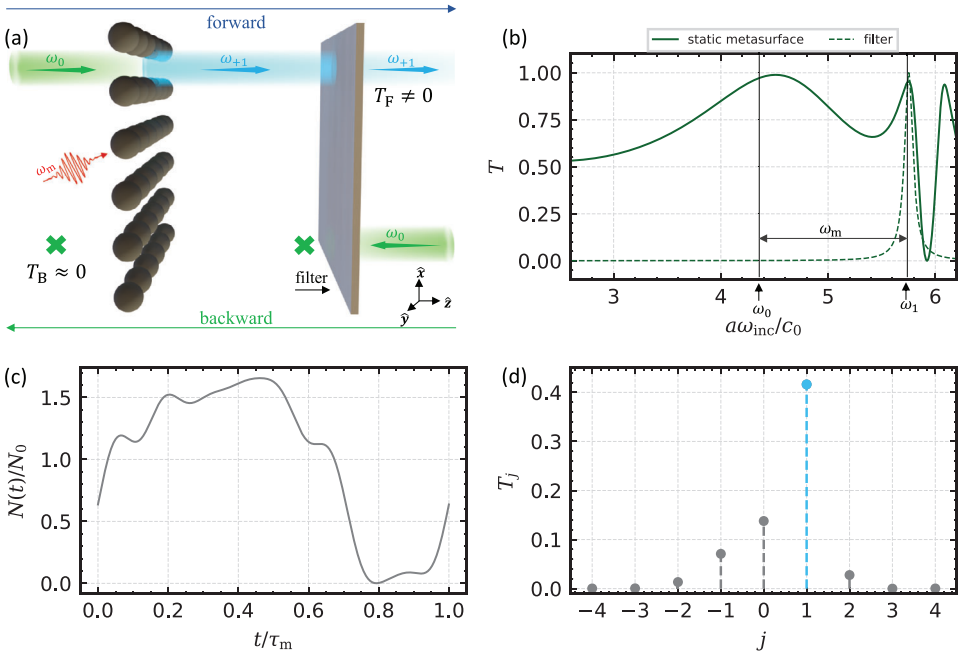

Figure 4. Asymmetric transmission (AT) of light at visible frequencies. a) A conceptual illustration of an AT system formed by cascading a spatiotemporal metasurface and a narrow-band filter. Here, T_F (T_B) corresponds to the final forward (backward) transmissivity of the AT system. b) The transmissivity T of the metasurface under static operation (solid curve) and filter (dotted curve) as shown in (a) as a function of the incident frequency ω_{inc}. c,d) The optimized electron density $N(t)$ as a function of time t, and the corresponding transmissivity contribution T_j of the spatiotemporal metasurface as a function of the harmonic number j, respectively.

When an electromagnetic wave at frequency ω_0 is incident to the system from the left-hand side (forward propagation), it encounters the spatiotemporal metasurface that upconverts most of its energy to an electromagnetic wave at frequency $\omega_1 = \omega_0 + \omega_m$. Our design objective is to render this upconversion efficient. The wave then encounters the filter that offers complete transmission to fields with frequency ω_1 while blocking all other frequencies.[82,83] Therefore, the wave at frequency ω_1 gets completely transmitted through the filter, leading to a non-zero final forward transmissivity T_F. On the other hand, if a wave at frequency ω_0 is incident from the right-hand side to the system (backward propagation), it encounters the filter first, which does not allow any further propagation of the wave. Therefore, the final backward transmissivity T_B of the whole system is negligible. Moreover, it is important to mention that the problem of frequency upconversion using spatiotemporal structures was also studied in various other works.[26,84–89] However, all these works were limited to the adiabatic regime of temporal modulation (i.e., $\omega_m \ll \omega_0$), which requires the use of frequency filters with very narrow bandwidths. Furthermore, the frequency of operation in these works was either in the microwave or infrared regime. In our framework, we use non-adiabatic temporal modulation, our metasurface operates at visible frequencies, and we fully take into account the effects of material dispersion that cannot be ignored for most of the materials at such frequencies.

We aim to design an AT system as shown in Figure 4a. A critical component of the AT system is the spatiotemporal metasurface, which is capable of frequency upconversion. In what follows, we discuss the choice of parameters of the system deemed to be supportive in achieving an efficient frequency upconversion using the Mie resonances of the underlying static metasurface.[60,90] To begin with, we assume the metasurface to be made from a square lattice of spheres. The radius R of the spheres is $R = 150$ nm, and the lattice constant a of the metasurface is $a = 2.6R$. Besides, for simplicity, the parameters are chosen such that the metasurface is subwavelength in the spectral range of interest. For a subwavelength metasurface, only the principle spatial diffraction order is propagating. The transmissivity T of the metasurface as a function of the incident frequency ω_{inc} under static conditions (i.e., $N(t) = N_0$) is shown in Figure 4b. Note that here, and for the following simulations, we assume a monochromatic x-polarized plane wave normally incident on the metasurface for calculating T. From Figure 4b, we observe that the static metasurface supports various Mie resonances.[90]

Using the transmission spectrum of the static metasurface, we choose the frequencies ω_0 and ω_m for the time-varying operation (see Figure 4b). From Figure 4b, it is apparent that ω_0 and ω_m are chosen such that ω_1 lies at a high-quality resonance of the static metasurface. Such a choice is made so that upon temporal modulation of the metasurface with an appropriately chosen $N(t)$, a resonant enhancement of the transmitted field occurs at ω_1 for an incident field at ω_0. Importantly, to design the AT functionality of the spatiotemporal metasurface for visible frequencies, the parameters a, R, and ω_m are chosen such that ω_0 and ω_1 lie in the visible spectrum. In our example, $\omega_0 = 2\pi \times 542$ THz and $\omega_1 = 2\pi \times 704$ THz.

Next, we use our inverse design framework to optimize the time-varying electron density $N(t)$ of the spatiotemporal metasurface. The total transmissivity T of the spatiotemporal metasurface can be written as a sum of the contribution of all the

transmitted frequency harmonics, i.e., $T = \sum_j T_j$[43] (see Figure 1a). Our goal is to maximize the transmissivity at ω_1. Therefore, we choose the objective function f_{obj} in terms of T_1 (see the Methods section).

The electron density $N(t)$ as a result of the optimization is shown in Figure 4c. Furthermore, the corresponding transmissivity contributions T_j as a function of the scattered harmonic number j are shown in Figure 4d. From Figure 4d, we observe that the metasurface with the optimal $N(t)$ preferentially transmits the energy of the incident wave to the frequency ω_1 (with $T_1 = 0.42$). Such a preferential transmission can be explained as follows. To begin with, the time-varying electron density $N(t)$ effectively modulates the amplitude and phase of the time-domain complex transmission coefficient of the metasurface[84] (see Section S7, Supporting Information). In principle, such a modulation of the transmission coefficient gives rise to the transmitted frequencies ω_j (with $j \in \mathbb{Z}$). However, due to the particular choice of f_{obj}, the optimizer converges such that this amplitude and phase modulation leads to an efficient coupling to ω_1 in transmission (also see Section S8, Supporting Information). Additionally, the high-quality resonance of the underlying static metasurface at ω_1 assists in the resonant enhancement of such a coupling (see Figure 4b). It is important to remark that such a preferential transmission is insensitive to the phase of the incident wave.

Note that the total transmission efficiency of the optimized spatiotemporal metasurface is about 66%. Approximately 15% of the incident energy is lost to reflection and about 19% to material losses due to frequency dispersion. Moreover, from Figure 4d, we observe that even though the maximum transmitted energy is linked to ω_1, a non-zero amount of energy is coupled to other scattered frequencies. To attain a perfect upconversion to the frequency ω_1 (i.e., $T_1 = 1$ and $T_j = 0 \forall j \neq 1$), one needs a spatiotemporal metasurface whose time-domain complex transmission coefficient has a pure linear phase modulation of 2π in the time-period τ_m[84] (see Section S7, Supporting Information). Attaining such an idealized condition is challenging at the optical frequencies.[91]

Next, we choose a filter that has almost unity transmissivity T at ω_1 and negligible T at all other frequencies (see the dotted curve in Figure 4b). We implement the filter by optimizing a Fabry-Perot cavity (see Section S9, Supporting Information). Other possible implementations of such a filter can be found in refs. [82, 83]. Finally, cascading such a filter with the optimized metasurface results in a final forward transmissivity of $T_F = 0.41562$ for a wave incident at $\omega_0 = 2\pi \times 542$ THz. Furthermore, the final backward transmissivity of the system for the same incident wave is $T_B = 0.00097$. Therefore, our inverse design framework allows us to realize the asymmetric transmission of light at visible frequencies.

It is important to mention that this AT is different from the phenomena of nonreciprocity.[92] We present a test of nonreciprocity for the cascaded in the Section S10 (Supporting Information). We perform this test by considering a backward propagating incident field to the filter at frequency ω_1. We find that since the electron density profile $N(t)$ in Figure 4c breaks the generalized time-reversal symmetry, the cascaded system is nonreciprocal.[93] Note that another trivial $N(t)$ profile known in the literature that leads to the breaking of the time-reversal symmetry and hence reciprocity is a sawtooth-type modulation.[84,85,93]

5. Conclusion

We have presented a differentiable T-matrix-based inverse design framework to engineer the scattering response of time-varying spheres and spatiotemporal metasurfaces on demand. These time-varying nanostructures are assumed to be made from a dispersive material with a time-varying electron density. Using our inverse design framework, we optimized the temporal profile of the electron density to tailor the desired functionality of the chosen nanostructure. We used a gradient-based approach to perform the optimization. We exploited our inverse design framework in two specific examples.

First, we computed the decay rate enhancement of dipoles kept near time-varying spheres. In particular, we optimized time-varying spheres such that the dipoles exhibit anomalous Drexhage effect. Next, we applied our inverse design framework to spatiotemporal metasurfaces. We optimized the metasurface to achieve an efficient frequency upconversion. Such an optimized metasurface is then cascaded with a narrow-band filter so that the composite system supports asymmetric transmission (AT) of light at visible frequencies. This AT operation is achieved while using non-adiabatic temporal modulation and considering the effects of material dispersion.

The T-matrix-based inverse design tool introduced in this article assists in simultaneously controlling the spatial and temporal properties of light. Depending on the choice of the objective function, various applications using the time-varying nanostructures can be realized in principle. From this perspective, our approach unlocks the opportunities to design novel photonic time and space-time crystals.

6. Methods Section

Further Details on the Differentiable T-Matrix Method: Assume a general polychromatic incident excitation to the considered time-varying nanostructure with frequencies, $\omega_j = \omega + j\omega_m$ with $j \in [-J, J]$. Here, J is an integer that should be chosen sufficiently large to ensure numerical convergence. Then, the incident field $\mathbf{E}^{\text{inc}}$ and scattered field $\mathbf{E}^{\text{sca}}$ can be written as

$$\mathbf{E}^{\text{inc}}(\mathbf{r}, t) = \sum_{jl\mu s} A^{\text{inc}}_{jl\mu s} \mathbf{F}^{(1)}_{j\mu s}(k_j \mathbf{r}) e^{-i\omega_j t} \tag{6}$$

$$\mathbf{E}^{\text{sca}}(\mathbf{r}, t) = \sum_{jl\mu s} A^{\text{sca}}_{jl\mu s} \mathbf{F}^{(3)}_{l\mu s}(k_j \mathbf{r}) e^{-i\omega_j t} \tag{7}$$

where $k_j = \omega_j / c_0$. Besides, $\mathbf{F}^{(1)}_{l\mu s}(x)$ ($\mathbf{F}^{(3)}_{l\mu s}(x)$) represent the regular (radiating) vector spherical harmonics (VSHs) with total angular momentum $l = 1, 2, 3..., l_{\max}$, z-component of angular momentum $\mu = -l, -l+1, ..., l$, and parity $s = 0, 1$. Here, $s = 0$ represents the transverse-electric (TE), and $s = 1$ represents the transverse-magnetic (TM) mode, respectively. Moreover, $l_{\max}$ is the maximum multipolar order retained in the expansion. It should be chosen sufficiently large to ensure numerical convergence. Next,

using the method in refs. [42, 43], one can connect $\mathbf{A}^{inc}$ and $\mathbf{A}^{sca}$ by the T-matrix $\mathbf{T}$ as given in Equation (1). Note that $\mathbf{T}$ is a square matrix with size $2l_{max}(2J+1)(l_{max}+2)$.

The Objective Function for Maximizing γ_{rad}/γ_0: From Equation (5), we observe that γ_{rad} is proportional to P_{far}. Therefore, maximizing γ_{rad} requires the maximization of P_{far}. For the simulation result shown in Figures 3c,d, the minimization of the objective function was found to perform better in terms of convergence. Therefore, the objective function, which needs to be minimized, is defined as $f_{obj}(\mathbf{M}) = w/P_{far}(\mathbf{M}) + (1-w)p(\mathbf{M})$. Here, $p(\mathbf{M})$ is a penalty function that penalizes the optimizer if it goes toward those values of $\mathbf{M}$ that correspond to a negative $N(t)$ for any $t \in [0, \tau_m]$ (see Subsection 3.2, Supporting Information, for more details on $p(\mathbf{M})$). Furthermore, w is a quantity that distributes the weight of the objective function between $1/P_{far}$ and the penalty p. We chose $w = 0.99$ for this optimization.

The Objective Function for Maximizing T_1: For the example shown in Figure 4a, T_1 needs to be maximized. Therefore, the objective function, which needs to be maximized, is defined as $f_{obj}(\mathbf{M}) = wT_1(\mathbf{M}) - (1-w)p(\mathbf{M})$. Here, as we are maximizing f_{obj}, $p(\mathbf{M})$ has a negative weight. Furthermore, $w = 0.84$ was chosen for this optimization.

Supporting Information

Supporting Information is available from the Wiley Online Library or from the author.

Acknowledgements

The authors would like to thank Dr. Elli Stamatopoulou, and Dr. Markus Nyman for useful discussions about the decay rate enhancement. P.G. and C.R. are part of the Max Planck School of Photonics, supported by the Bundesministerium für Bildung und Forschung, the Max Planck Society, and the Fraunhofer Society. P.G. acknowledges support from the Karlsruhe School of Optics and Photonics (KSOP). P.G. and C.R. acknowledge financial support by the German Research Foundation within the SFB 1173 (Project-ID No. 258734477). J.D.F. and C.R. acknowledge financial support by the Helmholtz Association in the framework of the innovation platform "Solar TAP". C.R. acknowledges support from the German Research Foundation within the Excellence Cluster 3D Matter Made to Order (EXC 2082/1 under project number 390761711) and by the Carl Zeiss Foundation. T.J.S. acknowledges funding from the Alexander von Humboldt Foundation. M.S.M. acknowledges support from the Research Council of Finland (Grant No. 336119). V.A. acknowledges the Research Council of Finland (Project No. 356797), Finnish Foundation for Technology Promotion, and Research Council of Finland Flagship Programme, Photonics Research and Innovation (PREIN), decision number 346529, Aalto University. X.W. acknowledges the Fundamental Research Funds for the Central Universities, China (Project No. 3072024WD2603) and the Scientific Research Foundation, Harbin Engineering University, China (Project No. 0165400209002).

Open access funding enabled and organized by Projekt DEAL.

Conflict of Interest

The authors declare no conflict of interest.

Data Availability Statement

The data that support the findings of this study are available from the corresponding author upon reasonable request.

Keywords

asymmetric transmission, decay rate enhancement, photonic inverse design, time-varying media

Received: September 9, 2024
Revised: December 6, 2024
Published online:

[1] N. Engheta, *Science* **2023**, *379*, 1190.
[2] E. Galiffi, R. Tirole, S. Yin, H. Li, S. Vezzoli, P. Huidobro, M. Silveirinha, R. Sapienza, A. Alù, J. Pendry, *Adv. Photonics* **2022**, *4*, 014002.
[3] G. Ptitcyn, M. S. Mirmoosa, A. Sotoodehfar, S. A. Tretyakov, *IEEE Antennas and Propagation Magazine* **2023**, *65*, 10.
[4] M. M. Asgari, P. Garg, X. Wang, M. S. Mirmoosa, C. Rockstuhl, V. Asadchy, *Adv. Opt. Photon.* **2024**, *16*, 958.
[5] J. R. Zurita-Sánchez, P. Halevi, J. C. Cervantes-González, *Phys. Rev. A* **2009**, *79*, 053821.
[6] X. Wang, P. Garg, M. Mirmoosa, A. Lamprianidis, C. Rockstuhl, V. Asadchy, *Nat. Photonics* **2024**, 1.
[7] A. Shaltout, A. Kildishev, V. Shalaev, *Opt. Mater. Express* **2015**, *5*, 2459.
[8] P. Huidobro, M. Silveirinha, E. Galiffi, J. Pendry, *Phys. Rev. Appl.* **2021**, *16*, 014044.
[9] M. Mirmoosa, M. Mostafa, A. Norrman, S. Tretyakov, *Phys. Rev. Res.* **2024**, *6*, 013334.
[10] X. Wang, V. Asadchy, S. Fan, S. Tretyakov, *ACS Photonics* **2021**, *8*, 3034.
[11] V. Pacheco-Peña, N. Engheta, *Light: Sci. Appl.* **2020**, *9*, 129.
[12] A. Akbarzadeh, N. Chamanara, C. Caloz, *Opt. Lett.* **2018**, *43*, 3297.
[13] X. Wang, M. S. Mirmoosa, S. A. Tretyakov, *Nanophotonics* **2023**, *12*, 2813.
[14] D. Ramaccia, A. Toscano, F. Bilotti, *Opt. Lett.* **2020**, *45*, 5836.
[15] V. Pacheco-Peña, N. Engheta, *Optica* **2020**, *7*, 323.
[16] M. Mostafa, A. Díaz-Rubio, M. Mirmoosa, S. Tretyakov, *Phys. Rev. Appl.* **2022**, *17*, 064048.
[17] Z. Hayran, F. Monticone, *Phys. Rev. Appl.* **2024**, *21*, 044007.
[18] J. Yang, J. C. Ke, W. K. Cao, M. Z. Chen, Q. Cheng, V. Galdi, T. J. Cui, *Adv. Opt. Mater.* **2021**, *9*, 2101043.
[19] M. H. M. Mostafa, M. S. Mirmoosa, S. A. Tretyakov, *Nanophotonics* **2023**, *12*, 2881.
[20] D. Globosits, J. Hüpfl, S. Rotter, *Phys. Rev. A* **2024**, *110*, 053515.
[21] E. Lustig, O. Segal, S. Saha, E. Bordo, S. N. Chowdhury, Y. Sharabi, A. Fleischer, A. Boltasseva, O. Cohen, V. M. Shalaev, M. Segev, *Nanophotonics* **2023**, *12*, 2221.
[22] R. Tirole, S. Vezzoli, E. Galiffi, I. Robertson, D. Maurice, B. Tilmann, S. A. Maier, J. B. Pendry, R. Sapienza, *Nat. Phys.* **2023**, *19*, 999.
[23] H. Moussa, G. Xu, S. Yin, E. Galiffi, Y. Radi, A. Alù, *Nat. Phys.* **2023**, *19*, 863.
[24] X. Wang, M. S. Mirmoosa, V. S. Asadchy, C. Rockstuhl, S. Fan, S. A. Tretyakov, *Sci. Adv.* **2023**, *9*, eadg7541.
[25] E. Galiffi, G. Xu, S. Yin, H. Moussa, Y. Ra'di, A. Alù, *Nat. Phys.* **2023**, *19*, 1703.
[26] J. Sisler, P. Thureja, M. Grajower, R. Sokhoyan, I. Huang, H. Atwater, *Nat. Nanotechnol.* **2024**, 1.
[27] A. Harwood, S. Vezzoli, T. Raziman, C. Hooper, R. Tirole, F. Wu, S. Maier, J. Pendry, S. Horsley, R. Sapienza, *arXiv preprint arXiv:2407.10809* **2024**.
[28] S. Buddhiraju, A. Dutt, M. Minkov, I. A. D. Williamson, S. Fan, *Nat. Commun.* **2021**, *12*, 2401.
[29] L. Zhang, Z. R. Huang, X. Q. Chen, Y. N. Zheng, S. Liu, V. Galdi, T. J. Cui, *Adv. Funct. Mater.* **2024**, *34*, 2314110.

[30] S. Molesky, Z. Lin, A. Y. Piggott, W. Jin, J. Vucković, A. W. Rodriguez, *Nat. Photonics* **2018**, *12*, 659.
[31] T. J. Sturges, M. Nyman, S. Kalt, K. Pälsi, P. Hilden, M. Wegener, C. Rockstuhl, A. Shevchenko, *ACS Photonics* **2024**.
[32] O. Kuster, Y. Augenstein, C. Rockstuhl, T. J. Sturges, *Appl. Phys. Lett.* **2024**, *125*, 18.
[33] Y. Zhu, Y. Chen, S. Gorsky, T. Shubitidze, L. Dal Negro, *JOSA B* **2023**, *40*, 1857.
[34] J. Baxter, L. Ramunno, *Opt. Express* **2023**, *31*, 22671.
[35] J. Kim, D. Lee, S. Yu, N. Park, *Nat. Phys.* **2023**, *19*, 726.
[36] Y. Long, L. Zou, L. Yu, H. Hu, J. Xiong, B. Zhang, *Opt. Mater. Express* **2024**, *14*, 2032.
[37] N. H. Phi, H. N. Bui, S.-Y. Moon, J.-W. Lee, *Adv. Intell. Syst.* **2024**, *6*, 2300565.
[38] M. M. Sadafi, A. F. da Mota, H. Mosallaei, *Appl. Phys. Lett.* **2023**, *123*, 101702.
[39] M. Lobet, N. Kinsey, I. Liberal, H. Caglayan, P. A. Huidobro, E. Galiffi, J. R. Mejía-Salazar, G. Palermo, Z. Jacob, N. Maccaferri, *ACS photonics* **2023**, *10*, 3805.
[40] S. A. R. Horsley, E. Galiffi, Y.-T. Wang, *Phys. Rev. Lett.* **2023**, *130*, 203803.
[41] J. Baxter, A. Pérez-Casanova, L. Cortes-Herrera, A. Calà Lesina, I. De Leon, L. Ramunno, *Adv. Photonics Res.* **2023**, *4*, 2200280.
[42] G. Ptitcyn, A. Lamprianidis, T. Karamanos, V. Asadchy, R. Alaee, M. Müller, M. Albooyeh, M. S. Mirmoosa, S. Fan, S. Tretyakov, C. Rockstuhl, *Laser Photonics Rev.* **2023**, *17*, 2100683.
[43] P. Garg, A. G. Lamprianidis, D. Beutel, T. Karamanos, B. Verfürth, C. Rockstuhl, *Opt. Express* **2022**, *30*, 45832.
[44] P. Waterman, *Proc. IEEE* **1965**, *53*, 805.
[45] P. P. Ewald, *Ann. Phys.* **1921**, *369*, 253.
[46] D. Beutel, I. Fernandez-Corbaton, C. Rockstuhl, *Comput. Phys. Commun.* **2024**, *297*, 109076.
[47] P. I. Frazier, *arXiv preprint arXiv:1807.02811* **2018**.
[48] J. Kennedy, R. Eberhart, in *Proceedings of ICNN'95-International Conference on Neural Networks*, vol. *4*, IEEE, **1995**, p. 1942.
[49] S. Yu, X. Piao, N. Park, *Nat. Commun.* **2020**, *11*, 4842.
[50] W. Ma, Z. Liu, Z. A. Kudyshev, A. Boltasseva, W. Cai, Y. Liu, *Nat. Photonics* **2021**, *15*, 77.
[51] C. Yeung, D. Ho, B. Pham, K. T. Fountaine, Z. Zhang, K. Levy, A. P. Raman, *ACS Photonics* **2022**, *9*, 1577.
[52] T. W. Hughes, M. Minkov, I. A. Williamson, S. Fan, *ACS Photonics* **2018**, *5*, 4781.
[53] M. Blaber, M. Arnold, M. Ford, *J. Phys. Chem. C* **2009**, *113*, 3041.
[54] G. Mie, *Ann. Phys.* **1908**, *330*, 377.
[55] COMSOL, Comsol Multiphysics, https://www.comsol.com/comsol-multiphysics (accessed: December 2024).
[56] JCM, JCM suite: The simulation tool for nano-optics, https://jcmwave.com/ (accessed: December 2024).
[57] N. Asadova, K. Achouri, K. Arjas, B. Auguié, R. Aydin, A. Baron, D. Beutel, B. Bodermann, K. Boussaoud, S. Burger, M. Choi, K. M. Czajkowski, A. B. Evlyukhin, A. Fazel-Najafabadi, I. Fernandez-Corbaton, P. Garg, D. Globosits, U. Hohenester, H. Kim, S. Kim, P. Lalanne, E. C. L. Ru, J. Meyer, J. Mun, L. Pattelli, L. Pflug, C. Rockstuhl, J. Rho, S. Rotter, B. Stout, et al., *arXiv preprint arXiv:2408.10727* **2024**.
[58] N. Stefanou, I. Stefanou, E. Almpanis, N. Papanikolaou, P. Garg, C. Rockstuhl, *J. Opt. Soc. Am. B* **2023**, *40*, 2842.
[59] I. Stefanou, P. A. Pantazopoulos, N. Stefanou, *J. Opt. Soc. Am. B* **2021**, *38*, 407.
[60] E. Panagiotidis, E. Almpanis, N. Papanikolaou, N. Stefanou, *Adv. Opt. Mater.* **2023**, *11*, 2202812.
[61] J. Bradbury, R. Frostig, P. Hawkins, M. J. Johnson, C. Leary, D. Maclaurin, G. Necula, A. Paszke, J. VanderPlas, S. Wanderman-Milne, Q. Zhang, JAX: composable transformations of Python+NumPy programs, **2018**, http://github.com/google/jax (accessed: December 2024).
[62] C. C. Margossian, *WIREs Data Mining and Knowledge Discovery* **2019**, *9*, e1305.
[63] M. Pelton, *Nat. Photonics* **2015**, *9*, 427.
[64] P. E. Stamatopoulou, C. Tserkezis, *OSA Continuum* **2021**, *4*, 918.
[65] E. Stamatopoulou, *Syddansk Universitet. Det Tekniske Fakultet, SDU, Denmark* **2023**.
[66] V. Giannini, A. I. Fernández-Domínguez, S. C. Heck, S. A. Maier, *Chemical Reviews* **2011**, *111*, 3888.
[67] M. Lyuborav, L. Dikopoltsev, E. Lustig, Y. Sharabi, M. Segev, *Science* **2022**, *377*, 425.
[68] G. Calajò, L. Rizzuto, R. Passante, *Phys. Rev. A* **2017**, *96*, 023802.
[69] J. Park, K. Lee, R.-Y. Zhang, H.-C. Park, J.-W. Ryu, G. Y. Cho, M. Y. Lee, Z. Zhang, N. Park, W. Jeon, J. Shin, C. T. Chan, B. Min, *arXiv preprint arXiv:2404.13287* **2024**.
[70] R. Yu, S. Fan, *Phys. Rev. Lett.* **2023**, *130*, 096902.
[71] S. Franke, J. Ren, M. Richter, A. Knorr, S. Hughes, *Phys. Rev. Lett.* **2021**, *127*, 013602.
[72] J. Ren, S. Franke, B. VanDrunen, S. Hughes, *Phys. Rev. A* **2024**, *109*, 013513.
[73] R. Citro, M. Aidelsburger, *Nature Reviews Physics* **2023**, *5*, 87.
[74] R. Carminati, J.-J. Greffet, C. Henkel, J. Vigoureux, *Optics Communications* **2006**, *261*, 368.
[75] A. Moroz, *Optics Communications* **2010**, *283*, 2277.
[76] K. Drexhage, *Journal of Luminescence* **1970**, *1-2*, 693.
[77] A. Krasnok, A. Slobozhanyuk, C. Simovski, S. Tretyakov, A. Poddubny, A. Miroshnichenko, Y. Kivshar, P. Belov, *Scientific reports* **2015**, *5*, 12956.
[78] L. Langguth, R. Fleury, A. Alù, A. F. Koenderink, *Phys. Rev. Lett.* **2016**, *116*, 224301.
[79] A. Kwadrin, A. F. Koenderink, *J. Phys. Chem. C* **2012**, *116*, 16666.
[80] A. Rahimzadegan, R. Alaee, C. Rockstuhl, R. W. Boyd, *Opt. Express* **2020**, *28*, 16511.
[81] A. S. Ansari, A. K. Iyer, B. Gholipour, *Nanophotonics* **2023**, *12*, 2639.
[82] M. Niraula, J. W. Yoon, R. Magnusson, *Opt. Lett.* **2015**, *40*, 5062.
[83] S. Tibuleac, R. Magnusson, *J. Opt. Soc. Am. A* **1997**, *14*, 1617.
[84] M. Liu, D. A. Powell, Y. Zarate, I. V. Shadrivov, *Phys. Rev. X* **2018**, *8*, 031077.
[85] Z. Wu, A. Grbic, *IEEE Trans. Antenn. Propagat.* **2020**, *68*, 1599.
[86] H. B. Sedeh, H. M. Dinani, H. Mosallaei, *Nanophotonics* **2022**, *11*, 4135.
[87] D. Ramaccia, D. L. Sounas, A. V. Marini, A. Toscano, F. Bilotti, *IEEE Antenn. Wireless Propag. Lett.* **2020**, *19*, 1886.
[88] T. T. Koutserimpas, R. Fleury, *Phys. Rev. Lett.* **2018**, *120*, 087401.
[89] Z. Yu, S. Fan, *Nat. Photonics* **2009**, *3*, 91.
[90] A. Rahimzadegan, T. D. Karamanos, R. Alaee, A. G. Lamprianidis, D. Beutel, R. W. Boyd, C. Rockstuhl, *Adv. Opt. Mater.* **2022**, *10*, 2102059.
[91] H. B. Sedeh, M. M. Salary, H. Mosallaei, *IEEE Access* **2020**, *8*, 185919.
[92] V. S. Asadchy, M. S. Mirmoosa, A. Díaz-Rubio, S. Fan, S. A. Tretyakov, *Proc. IEEE* **2020**, *108*, 1684.
[93] I. A. D. Williamson, M. Minkov, A. Dutt, J. Wang, A. Y. Song, S. Fan, *Proc. IEEE* **2020**, *108*, 10.